Biophysical *Journal*
Article

Biophysical Society

The Margination of Particles in Areas of Constricted Blood Flow

Erik J. Carboni,[1] Brice H. Bognet,[2] David B. Cowles,[1] and Anson W. K. Ma[1,2,*]
[1]Department of Chemical and Biomolecular Engineering and [2]Polymer Program, Institute of Materials Science, University of Connecticut, Storrs, Connecticut

ABSTRACT Stroke is a leading cause of death globally and is caused by stenoses, abnormal narrowings of blood vessels. Recently, there has been an increased interest in shear-activated particle clusters for the treatment of stenosis, but there is a lack of literature investigating the impact of different stenosis geometries on particle margination. Margination refers to the movement of particles toward the blood vessel wall and is desirable for drug delivery. The current study investigated ten different geometries and their effects on margination. Microfluidic devices with a constricted area were fabricated to mimic a stenosed blood vessel with different extent of occlusion, constricted length, and eccentricity (gradualness of the constriction and expansion). Spherical fluorescent particles with a diameter of 2.11 μm were suspended in blood and tracked as they moved into, through, and out of the constricted area. A margination parameter, *M*, was used to quantify margination based on the particle distribution after velocity normalization. Experimental results suggested that a constriction leads to an enhanced margination, whereas an expansion is responsible for a decrease in margination. Further, margination was found to increase with increasing percent occlusion and constriction length, likely a result of higher shear rate and longer residence time, respectively. Margination decreases as the stenosis geometry becomes more gradual (eccentricity increases) with the exception of a sudden constriction/expansion geometry. The findings demonstrate the importance of geometric effects on margination and call for detailed numerical modeling and geometric characterization of the stenosed areas to fully understand the underlying physics.

INTRODUCTION

Since 1997, stroke has been a leading cause of death globally (1,2). Although stroke in the gray matter of the brain is well known, ~30% of all strokes occur in the white matter (3). However, unlike the rest of the brain, in which the diameters of blood vessels can range from 15 to 140 μm with an average diameter of 30 μm, blood vessels in the white matter of the brain are arterioles and have diameters of ~100–200 μm (4–6). The narrowing of arterioles from the development of a stenosis is termed arteriolosclerosis and can cause strokes in the white matter, which can lead to dementia and motor function impairment, among other complications (3). Furthermore, lacunes are cavities that result from ruptured arteries of around 100 μm as a result of arteriosclerosis and can lead to death (7,8), and arteriolosclerosis can also be responsible for hypertension, chronic kidney disease, and left ventricular hypertrophy (9). Arterioles are an important part of the vasculature but have major differences from both tiny and large arteries.

Although blood behaves as a nearly Newtonian fluid in large blood vessels, in vessels with smaller diameters, such as the aforementioned arterioles, blood rheology becomes more complex, and a phenomenon known as margination can occur (10). In these smaller blood vessels that typically have diameters less than ~500 μm (11–13), interactions with red blood cells (RBCs) in the center of the vessel can cause particles to migrate to the periphery of the blood vessel or marginate (14). Although white blood cells were the first to be observed to marginate, drug-carrying microparticles were subsequently found to be able to also marginate (15,16). Margination of drug-carrying particles is important because marginated particles are near the wall and will be more effective in delivering their drug cargo. The extent of this margination depends on particle size, among many other characteristics of the particles and also the blood (17,18). However, whereas factors such as size, shape, and hematocrit and their effects on margination propensity have been investigated, the effects of stenoses on margination are largely unknown.

A number of studies have investigated drug delivery to a site of stenosis using specific attributes of the stenosis, such as the enhanced local shear (19–22). In this case, particle

Submitted October 18, 2017, and accepted for publication April 2, 2018.
*Correspondence: anson.ma@uconn.edu
Editor: Christopher Yip.
https://doi.org/10.1016/j.bpj.2018.04.010

margination becomes even more important because shear is at a maximum for marginated particles, which are closest to the blood vessel wall. However, stenoses can have various geometries, and there is a lack of understanding of the effects of stenosis geometry on the margination of drug-carrying particles, especially in the smaller arterioles. Additionally, although many studies have investigated the effects of various constriction and expansion geometries on RBC motion (8,23–39), platelet motion and thrombus formation (30,32,40–49), and microparticle concentration in the flow direction (50), the effect of stenosis geometry on the margination of drug-carrying particles remains largely unexplored. Indeed, no modeling or experimental studies exist that investigate particle margination for varying constriction geometries. It was previously observed that in regions of flow constriction, the margination propensity of microparticles may be affected (51). Despite these findings, it is unclear how exactly the geometry of a stenosis, which includes both an area of constriction and of expansion, affects microparticle margination. This is particularly relevant for in vitro margination studies, all of which tend to include flow constrictions and expansions in their experimental apparatus as a result of constrictions that are present in tubing-to-tubing or tubing-to-inlet-port connections.

In this study, multiple channel geometries were investigated in vitro via the use of microfluidic devices. The effects of percent occlusion, constriction length, and degree of eccentricity of the entrance and exit of the stenosis were investigated, and their effects on particle margination were quantified using direct particle tracking.

MATERIALS AND METHODS

Materials

Defibrinated bovine blood (Lampire Biological Laboratories, Pipersville, PA) was adjusted to 35% hematocrit using a washing procedure detailed in a previous study (51). Fluorescent polystyrene spheres of 2.11 μm diameter were suspended in the blood and used as model particles (Spherotech, Lake Forest, IL). This particle size was chosen because it falls within the size range of shear-activated nanoparticle aggregates, which use the enhanced local shear within a stenosis as the trigger for drug delivery (21). Also, this particle size displayed the most margination in the previous study and thus would be the most affected by subtle changes in the constriction and expansion geometry (51). For microfluidic device fabrication, polydimethylsiloxane (PDMS) prepolymer and curing agent were used (Silgard 184 Silicone Elastomer Kit; Krayden, Denver, CO).

Microfluidic device design

Microfluidic device designs were produced using AutoCAD software. Three geometric parameters, namely percent occlusion, constriction length, and eccentricity, were explored and varied one at a time. Percent occlusion is defined as the ratio of the change in channel width at the constricted area compared to the nonconstricted area. Three different percent occlusions (25, 50, and 75%), as illustrated in Fig. 1 *a*, were studied. The second parameter is constriction length and is defined as the distance between the end of constriction and the beginning of the expansion. Four constriction lengths, ranging from 50 μm to 10 mm, were investigated (Fig. 1 *b*). The third parameter is eccentricity, which describes the gradualness of channel constriction and expansion, as illustrated in Fig. 1 *c*. It should be noted that, unlike in some stenosis studies in which the eccentricity term refers to the degree to which a stenosis or lesion is off-centered (52,53), this work uses the mathematical definition of the term to describe the roundness of the corners or the gradualness of the constriction. In this study, eccentricity at the constriction and expansion is calculated according to the formula for the eccentricity of an ellipse:

$$\varepsilon = \sqrt{1 - \frac{b^2}{a^2}}, \tag{1}$$

where ε is the eccentricity, and a and b are the lengths of the semimajor and semiminor axes of the ellipse, respectively. This eccentricity refers to the shape of the entrance and exit of the constriction. As illustrated in Fig. 1, *c* and *d*, an eccentricity of 0 indicates that the constriction entrance and exit are in the shape of a quarter-circle, whereas higher eccentricities indicate that these shapes are elliptical and approaching a parabolic shape, which has an eccentricity of 1. A maximal eccentricity of $\varepsilon = 0.99$ was selected to limit the transition length required to establish full constriction. It should be noted that, in this study, the baseline geometry was arbitrarily chosen to have 50% occlusion, 10 mm length, and $\varepsilon = 0$, as denoted by the orange boxes in Fig. 1. Only one parameter was varied at a time. Fig. 1 lists which parameters were kept constant and which parameter was varied in each section. All devices used in this study have a channel depth of 100 μm and a channel width of 100 μm in the nonconstricted area. As shown in Fig. 2 *a*, the channel is 10 mm long both before and after the constricted area, whereas the constriction length varies. Concentric, axisymmetric constrictions were chosen to simplify the subsequent analysis on quantifying margination propensity (Quantifying Margination Propensity). Real stenoses vary considerably in geometry and likely deviate from such model designs. The effect of stenosis symmetry on margination is beyond the scope of this study and has not been investigated. However, previous studies on coronary artery stenoses suggest that stenosis asymmetry is associated with a longer recirculation length, but its impact on hemodynamics becomes negligible if the stenosis is far from a bifurcation (52,53).

Device fabrication

Microfluidic devices were fabricated from a silicon wafer master (FlowJEM, Toronto, Canada) using PDMS. Briefly, a PDMS elastomer base and a curing agent were mixed in a 10:1 ratio. The resultant mixture was poured over the master and degassed for 10 min to remove air bubbles and then placed in an oven and allowed to cure. The devices were cut out and punched to form an inlet and an outlet and then plasma-bonded (Basic Plasma Cleaner PDC-32G; Harrick Plasma, Ithaca, NY) to a glass coverslip (#1.5; Thermo Fisher Scientific, Waltham, MA).

Experimental setup

Blood containing the fluorescent 2.11 μm spherical particles was pumped through microfluidic devices using a pressure-driven pump system equipped with a flow controller (Fluigent, Villejuif, France). This pump system, instead of a syringe pump, was used for better flow rate control (51). The fluid was pumped through the microfluidic device at a physiologically relevant average velocity of 1 mm/s in the nonconstricted regions, which corresponds to a volumetric flow rate of 0.60 μL/min and an apparent wall shear rate of 77.9 s^{-1} (see Supporting Materials and Methods, Section 2) (54–57). The Reynolds number (Re number) is defined as follows:

$$\mathrm{Re} = \frac{\rho w \overline{u}}{\mu} = \frac{\rho Q}{\mu d}, \tag{2}$$

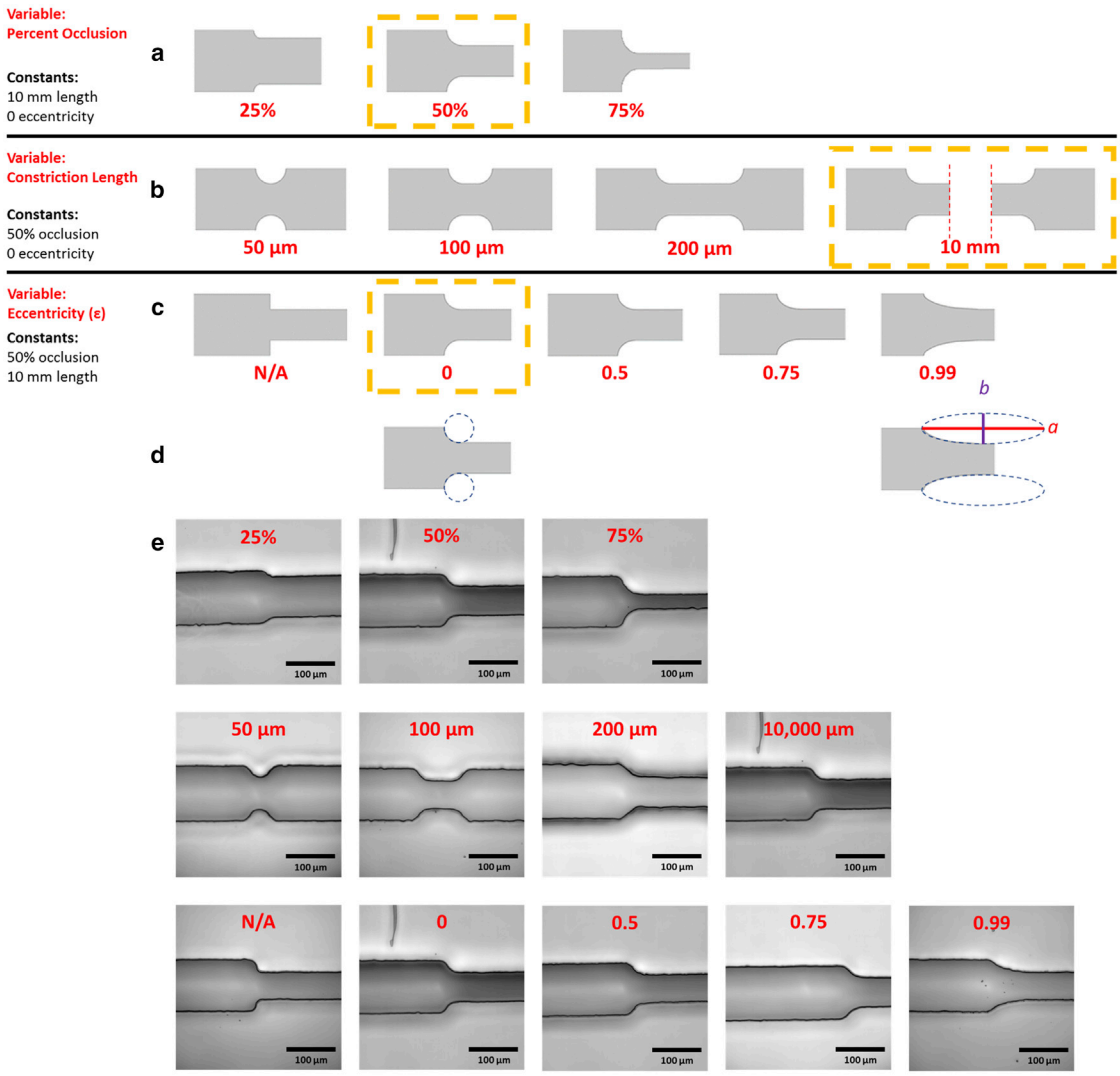

FIGURE 1 Three experimental parameters were explored and varied: (*a*) percent occlusion, (*b*) constriction length with mirrored expansion after the given distance, and (*c*) eccentricity (ε). The devices in orange boxes are the same baseline devices, with 50% occlusion, 10 mm length, and $\varepsilon = 0$. (*d*) Illustrations of the definition of eccentricity in this study, defined mathematically by the semimajor axis a and semiminor axis b, are shown to quantify the gradualness of the constriction entrance or exit. Pictured with circular and elliptical overlays for clarity are the $\varepsilon = 0$ channel (*quartercircle*-shaped entrance) and the $\varepsilon = 0.99$ channel (*elliptical* and nearly *parabolic*). (*e*) Transmitted light images of the microfluidic devices are shown for each different geometry at the location of the constriction. To see this figure in color, go online.

where ρ is the density ($= 1060$ kg/m^3), w is the channel width ($= 100$ μm), $\overline{u}$ is the mean fluid velocity ($= 1$ mm/s), μ is the (dynamic) viscosity of the fluid ($= 3.5$ mPa s), Q is the volumetric flow rate ($= 0.6$ μL/min), and d is the depth of the channel ($= 100$ μm). The Re number compares inertial forces to viscous forces and was calculated to be ~0.030, suggesting that viscous forces dominate inertial forces and that the flow is laminar for all device geometries. Alternatively, Eq. 2 can be written in terms of volumetric flow rate (Q) and channel depth (d). The volumetric flow rates and channel depth are kept constant in all experiments, and the Re number therefore remains constant if a Newtonian fluid is assumed. However, this simplified Re calculation does not take into account the shear-thinning nature of blood. A generalized Re number for a power law fluid was defined by several authors (58,59) as follows:

$$\mathrm{Re}_{genPL} = \frac{\rho w^n \overline{u}^{(2-n)}}{K((3n+1)/(4n))^n 8^{(n-1)}}, \qquad (3)$$

where n is the power law index of the fluid, and K is the flow consistency index of the fluid. Eq. 3 reduces to Eq. 2 for a Newtonian fluid with $n = 1$ and $K = \mu$. Using literature values for blood ($n = 0.716$ and $K = 0.0171$ Pa $\cdot$ s^n) (60), Re_{genPL} was calculated to be ca. 0.020 for the nonconstricted channel and 0.024, 0.030, and 0.044 for 25, 50, and 75% occlusion, respectively. Small Re numbers like these imply that viscous forces are dominant in the current experimental system.

For each device, a 60,000-frame (~7.5 min) time-lapse video was acquired using a dry objective lens (40×) with a high-speed camera (Andor iXon Ultra 897 iX0897 electron-multiplying charge-coupled device, 130 frames/s; Andor Technology, Belfast, UK) and an inverted fluorescence microscope (Nikon Eclipse Ti-E; Nikon Instruments, Melville, NY) with an epifluorescence source (Intensilight C-HGFIE, Nikon Instruments). These time-lapse videos were collected at four positions: 1) before the constriction, 2) after the constriction, 3) before the expansion, and 4) after the expansion. In each case, the time-lapses were collected 200 μm away

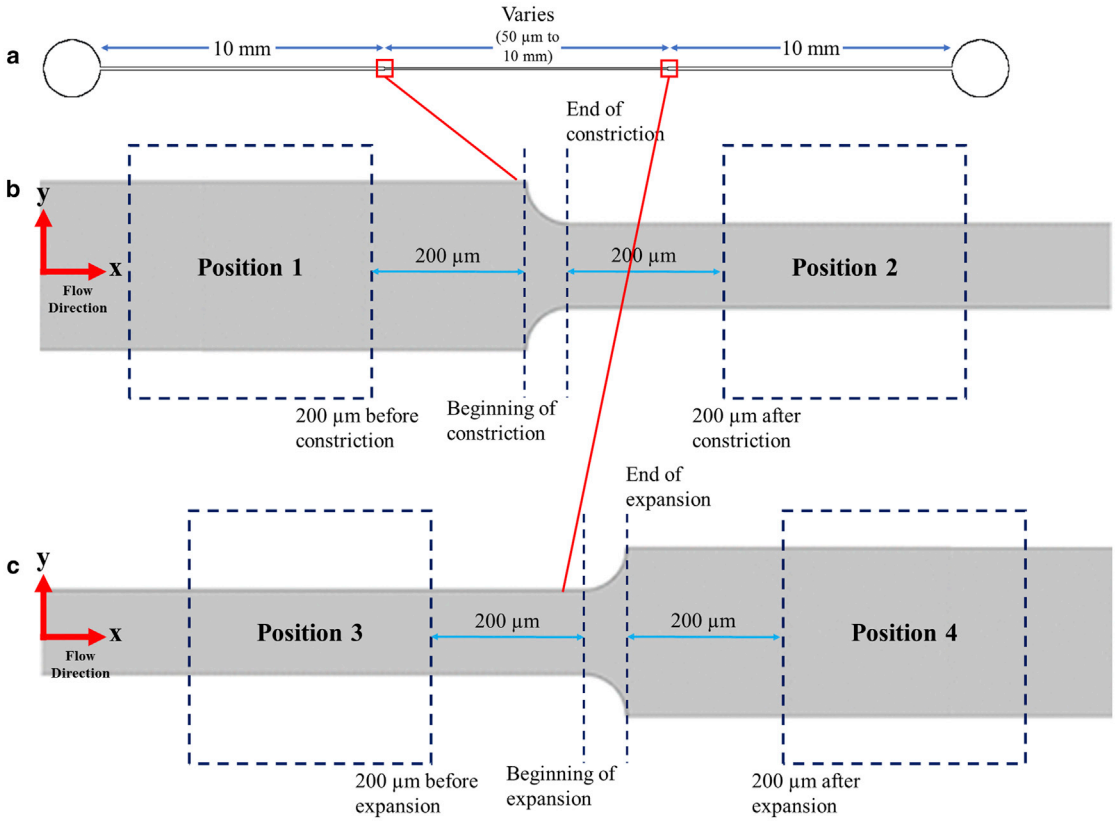

FIGURE 2 (*a*) Design of a typical device with 10 mm segments before and after a 10 mm constricted middle segment (devices with constriction length variations had shorter constricted segments). (*b*) A closeup of the first red box shows imaging positions 1 and 2. (*c*) A closeup of the second red box shows imaging positions 3 and 4. To see this figure in color, go online.

from the respective geometric changes to allow for flow reestablishment. Bright-field images of blood flow were also collected and averaged over time in an attempt to quantify the cell-free layer thickness. However, the cell-free layer was not clearly discernible, possibly because of the limited optical resolution and the current channel design. Fig. 2, *a–c* shows the areas of imaging for each full-length (10 mm) constriction device, with positions 3 and 4 located downstream and mirroring positions 2 and 1, respectively. Sample videos at each imaging position may be viewed as part of the Supporting Materials and Methods (explanation of videos contained in Section 1). It should be noted that, for the case of variable constriction length, videos at positions 2 and 3 were not collected because the lengths studied were shorter than the viewing window, and as a result, videos at these positions were impossible to obtain. As such, only the results at positions 1 and 4 were recorded for these devices. After each time-lapse video was collected, the reservoir of blood was gently shaken to keep the solution well mixed, and the device was perfused at a high flow rate (~8 μL/min) for ~2 min. After every 2–3 time-lapse video acquisitions, the entire system was flushed for 10 min before collecting the next time-lapse.

Image analysis: particle tracking

MATLAB (The MathWorks, Natick, MA) was used to analyze the time-lapse videos. The fluorescent particles were tracked using code developed in-house, as reported in (51). The tracking code consists of three steps. First, a background correction was performed to remove any stationary bright pixels associated with particles adhered to the bottom or sides of the channel. Second, the positions and sizes of all particles were calculated using a gradient-based method. The calculated particle size was used to eliminate out-of-focus particles based on their apparent larger size. Lastly, the positions of all remaining particles were tracked as a function of time to calculate velocities.

RESULTS AND DISCUSSION

Quantifying margination propensity

The methodology for the quantification of margination propensity is detailed in a previous study by the authors (51). Briefly, the channel in each time-lapse video was first split into 10 equally spaced segments, and the particles were tracked and counted in each of the 10 segments. The weighting by velocity was done to account for the naturally higher particle count near the center of the channel due to the higher velocity of the fluid and, therefore, throughput of particles. Because more particles will be seen nearer to the center of the channel, where the velocity is at a maximum and more particles will be observed over a given time for a uniform dispersion, weighting the particles based on their velocities allows for velocity profile normalization. This weighting is given by the following equation (51):

$$P_{i^{th}segment\in[1,10]} = \sum_{j\in[1,N]} \frac{v_{x,max}}{v_{x,j}}, \quad (4)$$

where $P_{i^{th}-segment}$ is the total weighted particle count for the i^{th} segment, $v_{x,max}$ is the maximal particle velocity across the channel, $v_{x,j}$ is the velocity of the j^{th} particle within the i^{th} segment, and N is the total number of particles within the i^{th} segment. From Eq. 4, each particle in a segment is assigned a weighted value, and slower particles will be weighted more heavily. The margination parameter, M, can be defined as follows:

$$M = \frac{P_{1^{st}segment} + P_{10^{th}segment}}{\sum_{i^{th}segment \in [1,10]} P_i}. \quad (5)$$

Eq. 5 allows for results that are easily interpretable and comparable. Assuming an even distribution of particles in a fluid where no margination occurs, such as water, M should be equal to 0.20 because the weighting would result in each segment having 10% of the total particle weight and two of the segments being adjacent to the channel wall. As expected, an M of ~0.20 was found for a control experiment that was conducted using water, as shown in Fig. 3 *a*. Larger values of M are indicative of marginating behavior, and the magnitude of M can be compared between experiments to quantify the effects of each of the geometrical changes studied on particle margination. For each experiment, an average M was calculated after tracking and analyzing thousands of particles, and a one-way analysis of variance (ANOVA) with a Tukey comparison was run on the results to ensure statistical significance.

Effect of position

For particles suspended in water, minimal changes in M were observed with varying position, as shown in Fig. 3 *a*. A one-way ANOVA has shown that none of these margination parameters are statistically significant from one another ($p > 0.05$ in all cases). This is as expected because there are no particle-RBC interactions in water, and these values are all very close to the expected value of 0.20 for a fluid with an even distribution of particles after velocity normalization. Fig. 3 *b* shows the results for blood in the same device at various positions. A one-way ANOVA shows that all of these values are statistically significant from one another ($p < 0.05$). M increases from position 1 to position 2 and from position 2 to position 3. However, a decrease in M is observed from position 3 to position 4. This trend was observed for all device geometries with the exception of the shorter length devices (50, 100, and 200 μm), where positions 2 and 3 are undefined (all average values and SDs are included in Tables S1 and S2, respectively, in Supporting Materials and Methods). It was considered that particles in the constriction are more difficult to track because of their faster velocities and that this could in turn artificially inflate M at positions 2 and 3, leading to the observed increase from position 1 to position 2 and the decrease from position 3 to position 4. However, because the water results show no significant difference in M between positions, it is likely that the blood results are not a result of tracking difficulties and that, instead, the geometry is the cause of the change in M from location to location. It is further hypothesized that particle-RBC interactions—the driving force for margination (14,18,61,62)—are significantly altered by the constriction and the expansion geometries.

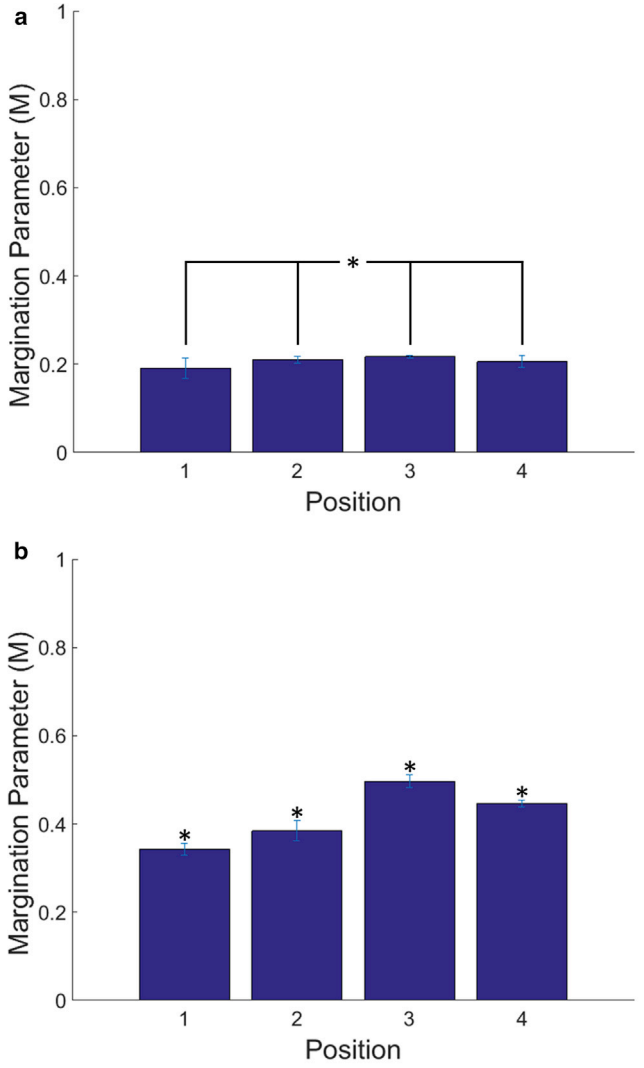

FIGURE 3 Margination parameters (M) at different positions for (*a*) water and (*b*) blood. Percent occlusion, 50%; constriction length, 10 mm; eccentricity, 0. Asterisks denote the significance of a value from all others, and asterisks with lines denote the nonsignificance of the grouped values from one another and the significance of nongrouped values. To see this figure in color, go online.

Effect of variable percent occlusion

As shown in Fig. 4, M increases with an increasing percent occlusion. These results were confirmed to be significant via the use of a one-way ANOVA ($p < 0.05$). The degree of

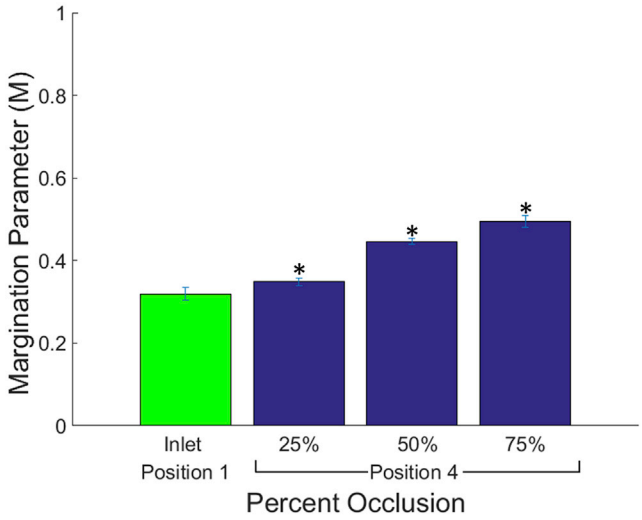

FIGURE 4 Margination parameter (M) results for the variable percent occlusion device. Length, 10 mm; eccentricity, 0. Asterisks denote the significance of a value from all others, and asterisks with lines denote the nonsignificance of the grouped values from one another and the significance of nongrouped values. To see this figure in color, go online.

occlusion appears to have a large effect on M. For instance, increasing percent occlusion from 25 to 75% results in a 41.6% increase in M. Blood is considered to be an incompressible fluid, and the mean velocity in the constricted region will change because of the reduction in the cross-sectional area of the channel, as given by the equation (63):

$$Q = \overline{u}A, \tag{6}$$

where Q is the volumetric flow rate, $\overline{u}$ is the mean velocity of the fluid, and A is the cross-sectional area of the channel. For the same volumetric flow rate, a reduction in the cross-sectional area of the channel results in a proportional increase in the velocity of the fluid. Occlusions of 25, 50, and 75% yield an increase in the wall shear rate by factors of 1.6, 3.3, and 13.0, respectively, relative to the nonconstricted channel (see Supporting Materials and Methods, Section S2, for detailed calculations). Other studies have linked higher shear rates to increased margination as a result of enhanced RBC-particle interactions (44,51,64,65). These interactions, which are between elastic and stiff particles and termed heterogeneous collisions, are identified as a driving force for margination (14,44,61,66). Indeed, a modeling study by Yazdani and Karniadakis, which investigated platelet margination for percent occlusions of both 50 and 75%, concluded that an increasing percent occlusion leads to an increasing shear rate and thus increased frequency of heterogeneous collisions that enhance the lateral drift of platelets toward channel walls (44). These results support the findings of this study and match the proposed explanation.

Effect of variable constriction length

As shown in Fig. 5, M increases with increasing constriction length. A one-way ANOVA showed that 50 and 200 μm lengths were significantly different, but 50 and 100 μm lengths and 100 and 200 μm lengths were not. This demonstrates that, although length does have an effect on M, the effect is difficult to see in 50–100 μm intervals. For the same percent occlusion of 50%, margination was found to increase with increasing length, likely as a result of the increased residence time for margination to occur. The distance required for an initially randomly placed particle to marginate, or the margination distance (X), is estimated to be 10.1 mm for the constricted channel, based on an adaption of an equation proposed by Zhao et al. (67):

$$X = \frac{\overline{u}\left(\frac{w}{4}\right)^2}{D_y},$$

where $\overline{u}$ is the average flow-direction velocity, w is the channel width ($w = 50$ μm for 50% occlusion), and D_y is the effective diffusivity in the y-direction (transverse to the flow direction). From a previous study (51), the effective diffusivity of a 2.11 μm particle, including RBC interactions, was experimentally found to be on the order of 15.42 $\mu m^2/s$. For an average velocity of 1 mm/s, the residence time required for margination to be completed is estimated to be 10.1 s, whereas the actual residence times for the 50, 100, 200, and 10,000 μm lengths are 50 ms, 100 ms, 200 ms, and 10 s, respectively. This simple analysis supports the residence time explanation but does not consider the effect of entrance or exit flows on margination.

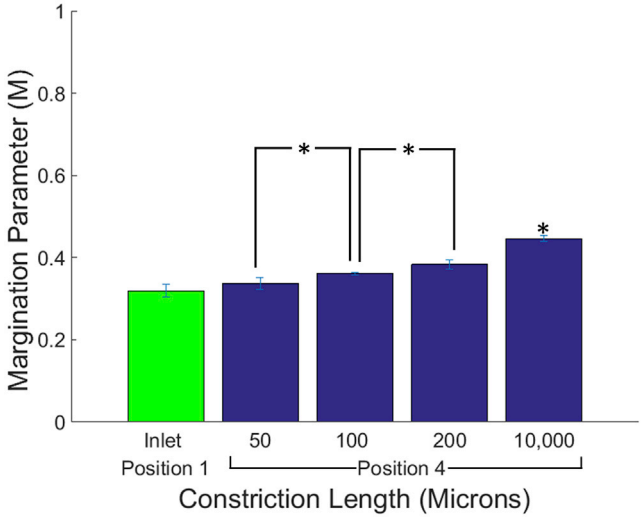

FIGURE 5 Margination parameter (M) results for the variable constriction length device. Percent occlusion, 50%; eccentricity, 0. Asterisks denote the significance of a value from all others, and asterisks with lines denote the nonsignificance of the grouped values from one another and the significance of nongrouped values. To see this figure in color, go online.

Interestingly, the effect of constriction length on margination does not appear to be linear. As constriction length increased from 50 to 200 μm (a fourfold increase), there was a 14% increase in M. However, increasing the length from 50 to 10,000 μm (a 200-fold increase in length) results in a 32% increase in M, which is equivalent to an additional increase of only 18% relative to the 200 μm case. Physiologically, although the lengths of cerebral arterioles in humans are known to be on the order of 3 mm (68), the length of a typical arteriolosclerotic region is not documented in the literature. If it is on the order of the length of a cerebral arteriole, however, then margination would be significant and would fall somewhere between the values of the 200 μm length channel and the 10,000 μm length channel.

Effect of variable eccentricity

Fig. 6 shows the effect of eccentricity (ε), or the gradualness of the occlusion, on margination. The larger the eccentricity value, the more gradual the change in channel width both at the entrance and exit of the stenosis. A one-way ANOVA showed significance ($p < 0.05$) of results for $\varepsilon = 0$ vs. $\varepsilon = 0.5$, whereas the other values were insignificant from one another but significant in comparison to $\varepsilon = 0$ and $\varepsilon = 0.5$. Margination was found to decrease as eccentricity increases, with one exception. In the case of a sudden change in geometry (ε = not applicable (N/A)), M is lower than the values of $\varepsilon = 0$ and $\varepsilon = 0.5$ but is comparable to those of $\varepsilon = 0.75$ and 0.99. These results for the N/A case, though puzzling, were confirmed through multiple experiments. Table 1 summarizes M at all four imaging positions (Fig. 2) for varying eccentricity values. M increases from position 1 to position 2 but decreases from position 3 to position 4 for all eccentricities. Compared with other eccentricities, ε = N/A has the largest percent increase in M from position 1 to position 2 (21%) but also the largest percent decrease in M from position 3 to position 4 (20%). The sudden constriction at the entrance has a positive effect on the margination that is largely counteracted by the negative effect of a sudden expansion at the exit of the stenosis. The degree of negation varies depending on the eccentricity.

TABLE 1 Percent Change in Margination Parameter for Varying Eccentricity

	Percent Change in Margination Parameter (M)		
Eccentricity	Position 1 to Position 2	Position 3 to Position 4	Position 1 to Position 4
ε = N/A	+21%	−20%	+8%
$\varepsilon = 0$	+12%	−10%	+30%
$\varepsilon = 0.5$	+3%	−4%	+26%
$\varepsilon = 0.75$	+5%	−5%	+21%
$\varepsilon = 0.99$	+2%	−6%	+11%

The percent change from position X to position Y is defined as $((M_Y - M_X)/M_X)$, where M_X and M_Y are the margination parameters at positions X and Y, respectively. A positive percent change indicates an increase in M, whereas a negative percent change is associated with a decrease in M.

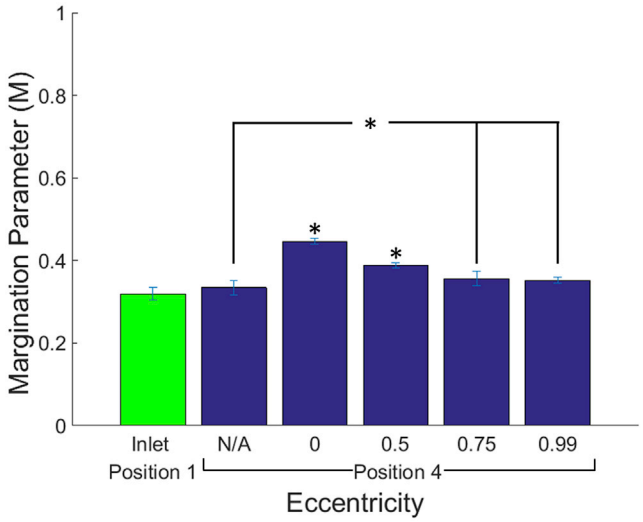

FIGURE 6 Margination parameter (M) results for the variable eccentricity device. Length, 10 mm; percent occlusion, 50%. Asterisks denote the significance of a value from all others, and asterisks with lines denote the nonsignificance of the grouped values from one another and the significance of nongrouped values. To see this figure in color, go online.

In the literature, some studies observed a recirculating flow after a sudden expansion (69,70). This recirculating flow was investigated for the ε = N/A device as a potential explanation for the unexpectedly low M observed. Recirculating flow was found to occur as a result of two competing lift forces arising from inertia: a shear-gradient lift force and a wall-effect lift force for particle Re numbers ($\mathrm{Re_p}$) greater than one, as given by the following equation:

$$\mathrm{Re}_p = \mathrm{Re}_{genPL}\left(\frac{a}{w}\right)^2, \tag{7}$$

where a is the particle diameter (2.11 μm), and w is the width of the channel. For $\mathrm{Re}_{genPL} = 0.020$ and $w = 100$ μm, Re_p was $\sim 8.95 \times 10^{-6}$, which is well outside of the range for recirculating flow, which tends to occur for Re_p values of order one or greater (69). Furthermore, no flow perturbations, such as a recirculating flow, were observed experimentally in the N/A eccentricity geometry after reviewing time-lapse videos taken at the constriction and expansion regions. Further, to better understand the flow profile of the N/A eccentricity device, blood was modeled as a homogenous power law fluid in COMSOL software, and the results are included in Supporting Materials and Methods, Section S3. Such an approach is inadequate at capturing margination, which originates from the interactions between RBCs and particles, but it did confirm the absence of recirculation. For future work, numerical models may be extended to offer insights into experimental

observations reported in this article for varying stenosis geometries, especially in the case of sudden constriction and expansion.

CONCLUSIONS

To summarize, particle margination was quantified via the direct tracking of fluorescent model particles in microfluidic devices with different constriction and expansion geometries. The margination parameter, or *M*, was calculated at different locations as the particles entered and exited the constricted areas mimicking a stenosed blood vessel. The higher the margination parameter, the larger the degree of margination. As a control experiment, particles were suspended in water and pumped through the devices. No signs of margination were recorded at any of the imaged positions. In the case of blood, *M* increased after a constriction but decreased after an expansion, suggesting that channel geometry has an important effect on particle margination. The effects of the degree of occlusion (or percent occlusion), constriction length, and the gradualness of constriction/expansion were further investigated. Increasing percent occlusion and increasing constriction length increased particle margination. As the percent occlusion increases, a higher shear rate is present in the constricted region, which has previously been shown to enhance margination (51,64). The positive effect of constriction length on margination is attributed to the longer residence time for longer constriction lengths. In terms of the channel shape, a more gradual constriction/expansion region (with increasing eccentricity) resulted in less degree of margination, with the exception of a sudden constriction/expansion geometry. No recirculating flows were observed experimentally or in COMSOL simulations. The exact reason is unclear and warrants further numerical modeling, such as particle dynamics simulations, which consider the discrete interactions between particles and RBCs. All in all, this study reveals that the channel geometry has nonnegligible effects on particle margination. However, percent occlusion, constriction length, and eccentricity are not well defined and are not fully characterized in existing in vivo studies. We hope this study will pave the way for more effective drug delivery to stenosed sites through an improved understanding of the contribution of margination to drug delivery at these sites (19–22). However, before this vision can be realized, more rigorous and detailed geometric characterizations of stenosed areas in vivo must be undertaken to better understand the underlying physics and typical stenosis shapes and sizes in various areas of the body. Taking atherosclerosis as a physiological example, myocardial infarctions are known to occur at percent occlusions above 70% (19,71). However, the cutoff value for a stenosis to become life threatening is largely unknown for arterioles. With combined geometric information and the results of this study, drug delivery to these sites can be better predicted, and future studies can isolate the effects of various particle characteristics from stenosis contributions to margination and drug delivery to these sites.

It should be noted that this experimental study did entail three major limitations. First, it was impossible to track individual RBCs and more importantly to visualize the potential interactions between RBCs and particles. Unlike modeling studies, this experimental study was only able to capture the aftereffects of these interactions. Second, the experimental results are greatly limited by the spatial and temporal resolution of the imaging system, whereas the exact positions of the particles are known in modeling studies (45,47,48,72). Given the experimental constraints, the margination is defined based on the normalized particle distribution at a given location instead of the exact particle trajectory, as in modeling studies. The results are therefore not directly comparable. Third, magnification must be sufficiently high to track the particles accurately, limiting the field of view to $\sim$200 μm in length and preventing particle tracking over longer distances. However, the experimental observations reported in this article reveal the important effect of channel geometry on particle margination and will inform further modeling studies.

SUPPORTING MATERIAL

Supporting Materials and Methods, one figure, three tables, and four videos are available at http://www.biophysj.org/biophysj/supplemental/S0006-3495(18)30450-8.

AUTHOR CONTRIBUTIONS

E.J.C. contributed to designing the research, performing the research, developing analytical tools, analyzing the data, and writing the article. B.H.B. contributed to developing the analytical tools. D.B.C. contributed to analyzing the early data. A.W.K.M. contributed to designing the research, analyzing the data, and writing the article.

ACKNOWLEDGMENTS

The authors thank Dr. Christopher O'Connell (University of Connecticut) for his microscopy expertise and Dr. Suzy Torti (University of Connecticut Health Center) for useful discussions and providing partial funding support for E.J.C.

This material is based on work supported by the Department of Defense Mentor-Predoctoral Fellow Research Award program under grant number W81XWH-10-1-0434, the National Science Foundation Graduate Research Fellowship under grant number DGE-1247393, the National Science Foundation under grant number 1250661, and the Graduate Assistance in Areas of National Need Fellowship (GAANN) under grant number P200A150330.

REFERENCES

1. Murray, C. J., and A. D. Lopez. 1997. Mortality by cause for eight regions of the world: Global Burden of Disease Study. *Lancet*. 349:1269–1276.

2. Wang, H.; GBD 2015 Mortality and Causes of Death Collaborators. 2016. Global, regional, and national life expectancy, all-cause mortality, and cause-specific mortality for 249 causes of death, 1980-2015: a systematic analysis for the Global Burden of Disease Study 2015. *Lancet.* 388:1459–1544.
3. Rosenzweig, S., and S. T. Carmichael. 2013. Age-dependent exacerbation of white matter stroke outcomes: a role for oxidative damage and inflammatory mediators. *Stroke.* 44:2579–2586.
4. Harnarine-Singh, D., G. Geddes, and J. B. Hyde. 1972. Sizes and numbers of arteries and veins in normal human neopallium. *J. Anat.* 111:171–179.
5. Alexander, L., and T. J. Putnam. 1938. Pathological alterations of cerebral vascular patterns. *Res. Publ. Assoc. Res. Nerv. Ment. Dis.* 18:471–543.
6. Rowbotham, G. F., and E. Little. 1965. Circulations of the cerebral hemispheres. *Br. J. Surg.* 52:8–21.
7. Fisher, C. M. 1965. Lacunes: small, deep cerebral infarcts. *Neurology.* 15:774–784.
8. Fujiwara, H., T. Ishikawa, …, T. Yamaguchi. 2009. Red blood cell motions in high-hematocrit blood flowing through a stenosed microchannel. *J. Biomech.* 42:838–843.
9. Kanbay, M., L. G. Sánchez-Lozada, …, R. J. Johnson. 2011. Microvascular disease and its role in the brain and cardiovascular system: a potential role for uric acid as a cardiorenal toxin. *Nephrol. Dial. Transplant.* 26:430–437.
10. Fedosov, D. A., B. Caswell, …, G. E. Karniadakis. 2010. Blood flow and cell-free layer in microvessels. *Microcirculation.* 17:615–628.
11. Carugo, D., L. Capretto, …, X. L. Zhang. 2013. A microfluidic-based arteriolar network model for biophysical and bioanalytical investigations. *Curr. Anal. Chem.* 9:47–59.
12. Lim, E. J., T. J. Ober, …, M. Toner. 2012. Visualization of microscale particle focusing in diluted and whole blood using particle trajectory analysis. *Lab Chip.* 12:2199–2210.
13. Pries, A. R., T. W. Secomb, and P. Gaehtgens. 1996. Biophysical aspects of blood flow in the microvasculature. *Cardiovasc. Res.* 32:654–667.
14. Kumar, A., and M. D. Graham. 2012. Mechanism of margination in confined flows of blood and other multicomponent suspensions. *Phys. Rev. Lett.* 109:108102.
15. Dutrochet, H. 1824. Recherches anatomiques et physiologiques sur la structure intime des animaux et des végétaux, et sur leur motilité. J. B. Baillière, Beauvais, France.
16. Segré, G., and A. Silberberg. 1962. Behaviour of macroscopic rigid spheres in Poiseuille flow Part 2. Experimental results and interpretation. *J. Fluid Mech.* 14:136–157.
17. Carboni, E., K. Tschudi, …, A. W. Ma. 2014. Particle margination and its implications on intravenous anticancer drug delivery. *AAPS PharmSciTech.* 15:762–771.
18. Kumar, A., and M. D. Graham. 2012. Margination and segregation in confined flows of blood and other multicomponent suspensions. *Soft Matter.* 8:10536–10548.
19. Holme, M. N., I. A. Fedotenko, …, A. Zumbuehl. 2012. Shear-stress sensitive lenticular vesicles for targeted drug delivery. *Nat. Nanotechnol.* 7:536–543.
20. Saxer, T., A. Zumbuehl, and B. Müller. 2013. The use of shear stress for targeted drug delivery. *Cardiovasc. Res.* 99:328–333.
21. Korin, N., M. Kanapathipillai, …, D. E. Ingber. 2012. Shear-activated nanotherapeutics for drug targeting to obstructed blood vessels. *Science.* 337:738–742.
22. Korin, N., M. Kanapathipillai, and D. E. Ingber. 2013. Shear-responsive platelet mimetics for targeted drug delivery. *Isr. J. Chem.* 53:610–615.
23. Vahidkhah, K., P. Balogh, and P. Bagchi. 2016. Flow of red blood cells in stenosed microvessels. *Sci. Rep.* 6:28194.
24. Akbar, N. S. 2016. Non-Newtonian model study for blood flow through a tapered artery with a stenosis. *Alexandria Engineering Journal.* 55:321–329.
25. Pinho, D., R. O. Rodrigues, …, R. Lima. 2014. Motion of rigid particles flowing in a microfluidic device with a pronounced stenosis: trajectories and deformation index. In 11th World Congress on Computational Mechanics, WCCM 2014, 5th European Conference on Computational Mechanics, ECCM 2014 and 6th European Conference on Computational Fluid Dynamics, ECFD 2014, pp. 6234–6240.
26. Monteiro, F. C., B. Taboada, and R. Lima. 2014. Visualization of red blood cells flowing through a PDMS microchannel with a microstenosis: an image analysis assessment. In Computational Vision and Medical Image Processing IV - Proceedings of Eccomas Thematic Conference on Computational Vision and Medical Image Processing, VIPIMAGE 2013, pp. 369–374.
27. Hall, C. L., and M. Calt. 2014. Computational modeling of thrombotic microparticle deposition in nonparallel flow regimes. *J. Biomech. Eng.* 136:111002–111002-10.
28. Srivastava, V. P., R. Rastogi, and R. Vishnoi. 2010. A two-layered suspension blood flow through an overlapping stenosis. *Comput. Math. Appl.* 60:432–441.
29. Li, H., H. Fang, …, S. Chen. 2004. Lattice Boltzmann simulation on particle suspensions in a two-dimensional symmetric stenotic artery. *Phys. Rev. E Stat. Nonlin. Soft Matter Phys.* 69:031919.
30. Zhao, R., J. N. Marhefka, …, J. F. Antaki. 2008. Micro-flow visualization of red blood cell-enhanced platelet concentration at sudden expansion. *Ann. Biomed. Eng.* 36:1130–1141.
31. Sousa, P. C., F. T. Pinho, …, M. A. Alves. 2011. Extensional flow of blood analog solutions in microfluidic devices. *Biomicrofluidics.* 5:14108.
32. Ha, H., and S. J. Lee. 2013. Hemodynamic features and platelet aggregation in a stenosed microchannel. *Microvasc. Res.* 90:96–105.
33. Yaginuma, T., M. S. N. Oliveira, …, T. Yamaguchi. 2011. Red blood cell deformation in flows through a PDMS hyperbolic microchannel. In Technical Proceedings of the 2011 NSTI Nanotechnology Conference and Expo, NSTI-Nanotech 2011, pp. 505–507.
34. Taboada, B., F. C. Monteiro, and R. Lima. 2016. Automatic tracking and deformation measurements of red blood cells flowing through a microchannel with a microstenosis: the keyhole model. *Comput. Methods Biomech. Biomed. Eng. Imaging Vis.* 4:229–237.
35. Faustino, V., D. Pinho, …, R. Lima. 2014. Flow of red blood cells suspensions through hyperbolic microcontractions. In Lecture Notes in Computational Vision and Biomechanics, pp. 151–163.
36. Kim, J., J. F. Antaki, and M. Massoudi. 2016. Computational study of blood flow in microchannels. *J. Comput. Appl. Math.* 292:174–187.
37. Zaman, A., N. Ali, and M. Sajid. 2017. Numerical simulation of pulsatile flow of blood in a porous-saturated overlapping stenosed artery. *Math. Comput. Simul.* 134:1–16.
38. Xiao, L. L., S. Chen, …, Y. Liu. 2014. Simulation of a single red blood cell flowing through a microvessel stenosis using dissipative particle dynamics. *Mol. Cell. Biomech.* 11:67–85.
39. Dimakopoulos, Y., G. Kelesidis, …, J. Tsamopoulos. 2015. Hemodynamics in stenotic vessels of small diameter under steady state conditions: effect of viscoelasticity and migration of red blood cells. *Biorheology.* 52:183–210.
40. Tovar-Lopez, F. J., G. Rosengarten, …, W. S. Nesbitt. 2013. An investigation on platelet transport during thrombus formation at micro-scale stenosis. *PLoS One.* 8:e74123.
41. Li, M., D. N. Ku, and C. R. Forest. 2012. Microfluidic system for simultaneous optical measurement of platelet aggregation at multiple shear rates in whole blood. *Lab Chip.* 12:1355–1362.
42. Bark, D. L., Jr., and D. N. Ku. 2013. Platelet transport rates and binding kinetics at high shear over a thrombus. *Biophys. J.* 105:502–511.
43. Kamada, H., K. Tsubota, …, T. Yamaguchi. 2011. Computational study on effect of stenosis on primary thrombus formation. *Biorheology.* 48:99–114.

44. Yazdani, A., and G. E. Karniadakis. 2016. Sub-cellular modeling of platelet transport in blood flow through microchannels with constriction. *Soft Matter.* 12:4339–4351.

45. Mehrabadi, M., D. N. Ku, and C. K. Aidun. 2015. A continuum model for platelet transport in flowing blood based on direct numerical simulations of cellular blood flow. *Ann. Biomed. Eng.* 43:1410–1421.

46. Yazdani, A., H. Li, …, G. E. Karniadakis. 2017. A general shear-dependent model for thrombus formation. *PLoS Comput. Biol.* 13:e1005291.

47. Mehrabadi, M., L. D. Casa, …, D. N. Ku. 2016. A predictive model of high shear thrombus growth. *Ann. Biomed. Eng.* 44:2339–2350.

48. Reasor, D. A., Jr., M. Mehrabadi, …, C. K. Aidun. 2013. Determination of critical parameters in platelet margination. *Ann. Biomed. Eng.* 41:238–249.

49. Westein, E., A. D. van der Meer, …, J. W. Heemskerk. 2013. Atherosclerotic geometries exacerbate pathological thrombus formation poststenosis in a von Willebrand factor-dependent manner. *Proc. Natl. Acad. Sci. USA.* 110:1357–1362.

50. Bächer, C., L. Schrack, and S. Gekle. 2017. Clustering of microscopic particles in constricted blood flow. *Phys. Rev. Fluids.* 2:013102.

51. Carboni, E. J., B. H. Bognet, …, A. W. K. Ma. 2016. Direct tracking of particles and quantification of margination in blood flow. *Biophys. J.* 111:1487–1495.

52. Pagiatakis, C., J. C. Tardif, …, R. Mongrain. 2017. Effect of stenosis eccentricity on the functionality of coronary bifurcation lesions-a numerical study. *Med. Biol. Eng. Comput.* 55:2079–2095.

53. Javadzadegan, A., Y. Shimizu, …, M. Ohta. 2013. Correlation between Reynolds number and eccentricity effect in stenosed artery models. *Technol. Health Care.* 21:357–367.

54. Kubota, K., J. Tamura, …, I. Nishio. 1996. The behaviour of red cells in narrow tubes in vitro as a model of the microcirculation. *Br. J. Haematol.* 94:266–272.

55. Cai, B., J. Fan, …, B. M. Fu. 2012. Adhesion of malignant mammary tumor cells MDA-MB-231 to microvessel wall increases microvascular permeability via degradation of endothelial surface glycocalyx. *J. Appl. Physiol.* 113:1141–1153.

56. Pries, A. R., T. W. Secomb, and P. Gaehtgens. 1995. Structure and hemodynamics of microvascular networks: heterogeneity and correlations. *Am. J. Physiol.* 269:H1713–H1722.

57. Klug, P. P., L. S. Lessin, and P. Radice. 1974. Rheological aspects of sickle cell disease. *Arch. Intern. Med.* 133:577–590.

58. Madlener, K., B. Frey, and H. K. Ciezki. 2009. Generalized reynolds number for non-newtonian fluids. *Progress in Propulsion Physics.* 1:237–250.

59. Metzner, A. B., and J. C. Reed. 1955. Flow of non-newtonian fluids—correlation of the laminar, transition, and turbulent-flow regions. *AIChE J.* 1:434–440.

60. Elblbesy, M. A., and A. T. Hereba. 2016. Computation of the coefficients of the power law model for whole blood and their correlation with blood parameters. *Appl. Phys. Rev.* 8:1.

61. Kumar, A., R. G. Henríquez Rivera, and M. D. Graham. 2014. Flow-induced segregation in confined multicomponent suspensions: effects of particle size and rigidity. *J. Fluid Mech.* 738:423–462.

62. Vahidkhah, K., and P. Bagchi. 2015. Microparticle shape effects on margination, near-wall dynamics and adhesion in a three-dimensional simulation of red blood cell suspension. *Soft Matter.* 11:2097–2109.

63. Bird, R. B., W. E. Stewart, and E. N. Lightfoot. 2007. Transport Phenomena. Wiley, Hoboken, NJ.

64. Charoenphol, P., R. B. Huang, and O. Eniola-Adefeso. 2010. Potential role of size and hemodynamics in the efficacy of vascular-targeted spherical drug carriers. *Biomaterials.* 31:1392–1402.

65. Namdee, K., A. J. Thompson, …, O. Eniola-Adefeso. 2013. Margination propensity of vascular-targeted spheres from blood flow in a microfluidic model of human microvessels. *Langmuir.* 29:2530–2535.

66. Kumar, A., and M. D. Graham. 2011. Segregation by membrane rigidity in flowing binary suspensions of elastic capsules. *Phys. Rev. E Stat. Nonlin. Soft Matter Phys.* 84:066316.

67. Zhao, H., E. S. G. Shaqfeh, and V. Narsimhan. 2012. Shear-induced particle migration and margination in a cellular suspension. *Phys. Fluids.* 24:011902.

68. Aydin, F., W. I. Rosenblum, and J. T. Povlishock. 1991. Myoendothelial junctions in human brain arterioles. *Stroke.* 22:1592–1597.

69. Sollier, E., D. E. Go, …, D. Di Carlo. 2014. Size-selective collection of circulating tumor cells using Vortex technology. *Lab Chip.* 14:63–77.

70. Dhar, M., E. Pao, …, D. Di Carlo. 2016. Label-free enumeration, collection and downstream cytological and cytogenetic analysis of circulating tumor cells. *Sci. Rep.* 6:35474.

71. Pijls, N. H. 2009. Acute myocardial infarction and underlying stenosis severity. *Am. J. Cardiol.* 103:1204–1205.

72. Mehrabadi, M., D. N. Ku, and C. K. Aidun. 2016. Effects of shear rate, confinement, and particle parameters on margination in blood flow. *Phys. Rev. E.* 93:023109.